

Spectrally Resolved Energy Dissipation Rate and Momentum Flux of Breaking Waves

JOHANNES R. GEMMRICH

University of Victoria, Victoria, British Columbia, Canada

MICHAEL L. BANNER

School of Mathematics and Statistics, The University of New South Wales, Sydney, New South Wales, Australia

CHRIS GARRETT

University of Victoria, Victoria, British Columbia, Canada

(Manuscript received 11 January 2007, in final form 16 October 2007)

ABSTRACT

Video observations of the ocean surface taken from aboard the Research Platform *FLIP* reveal the distribution of the along-crest length and propagation velocity of breaking wave crests that generate visible whitecaps. The key quantity assessed is $\Lambda(c)dc$, the average length of breaking crests per unit area propagating with speeds in the range $(c, c + dc)$. Independent of the wave field development, $\Lambda(c)$ is found to peak at intermediate wave scales and to drop off sharply at larger and smaller scales. In developing seas breakers occur at a wide range of scales corresponding to phase speeds from about $0.1 c_p$ to c_p , where c_p is the phase speed of the waves at the spectral peak. However, in developed seas, breaking is hardly observed at scales corresponding to phase speeds greater than $0.5 c_p$. The phase speed of the most frequent breakers shifts from $0.4 c_p$ to $0.2 c_p$ as the wave field develops. The occurrence of breakers at a particular scale as well as the rate of surface turnover are well correlated with the wave saturation. The fourth and fifth moments of $\Lambda(c)$ are used to estimate breaking-wave-supported momentum fluxes, energy dissipation rate, and the fraction of momentum flux supported by air-entraining breaking waves. No indication of a Kolmogorov-type wave energy cascade was found; that is, there is no evidence that the wave energy dissipation is dominated by small-scale waves. The proportionality factor b linking breaking crest distributions to the energy dissipation rate is found to be $(7 \pm 3) \times 10^{-5}$, much smaller than previous estimates.

1. Introduction

Surface waves have been described as the “gearbox” between the atmosphere and ocean (Ardhuin et al. 2005). In particular, wave breaking plays an important role in many air–sea exchange and upper-ocean processes. At moderate to high wind speeds the momentum transfer from wind to ocean currents passes through the wave field via wave breaking. The breaking of surface waves is responsible for the dissipation of wave energy, and thus wave breaking is a source of enhanced turbulence kinetic energy (TKE) in the near-surface layer. Breaking waves not only transfer energy, momentum, heat, and gases from the atmosphere to the

ocean surface layer, they also foster aerosol generation and latent heat flux due to sea spray. Breaking waves also disperse pollutants and generate underwater sound. Comprehensive overviews of the role of wave-induced turbulence in upper-ocean dynamics and air–sea exchange processes are given by Thorpe (1995), Melville (1996), and Duncan (2001).

Furthermore, wave breaking affects wave development as it dominates the dissipation of wave energy and controls wave growth. To improve our understanding of wave-breaking-related processes a twofold approach is necessary: (i) detailed process studies of energy dissipation rates, mixing, sound generation, etc. and (ii) knowledge of the occurrence and scale of wave breaking. Here we focus on the latter.

It is well known, even to the casual observer, that wave breaking occurs at a wide range of scales. The breaking scale is of great importance to all physical

Corresponding author address: J. Gemmrich, Institute of Ocean Sciences, P.O. Box 6000, Sidney, BC V8L 4B2, Canada.
E-mail: gemmrich@uvic.ca

processes associated with wave breaking. For example, a small-scale breaker dissipates less energy than a breaking dominant wave. Therefore, we are interested in the breaking probabilities of different wave scales,

$$P(\mathbf{c}) = \frac{N_{\text{brk}}(\mathbf{c}, \mathbf{c} + \Delta\mathbf{c})}{N_{\text{all}}(\mathbf{c}, \mathbf{c} + \Delta\mathbf{c})}, \quad (1)$$

where N_{brk} is the number of *breaking wave crests* propagating with velocities in the range $(\mathbf{c}, \mathbf{c} + \Delta\mathbf{c})$ passing a fixed point per unit time and N_{all} is the *total* number of *wave crests* propagating with velocities in the range $(\mathbf{c}, \mathbf{c} + \Delta\mathbf{c})$ passing a fixed point per unit time. Banner et al. (2002) found that above a common threshold level the breaking probability increases roughly linearly with normalized wave saturation

$$\sigma(\omega) = \frac{\omega^5 S(\omega)}{2g^2 D(\omega)}, \quad (2)$$

where ω is the wave frequency and $S(\omega)$ the wave height spectrum with the empirical angular spreading weight $D(\omega)$ (given in section 4). The breaking events were assigned to spectral bands ranging from the peak frequency ω_p up to approximately $2.5\omega_p$. For all bands, a clear threshold behavior was found with breaking starting at a common threshold $\sigma \approx 4.5 \times 10^{-3}$.

Defining multiscale breaking probabilities by Eq. (1) requires knowledge of the total number N_{all} of wave crests of a certain scale passing a fixed point. However, this measurement is not commonly available. A more practical measure was introduced by Phillips (1985). Realizing that the scale of a breaking wave may be partly represented by the length of the breaking crest and its propagation speed and direction, he defined $\Lambda(c, \theta)$, the spectral density of breaking wave crest length per unit area with speed c and propagation direction θ . Note that this is a measure of the length of the actively breaking crest perpendicular to the wave propagation, and thus does not give the whitecap area, which also depends on the swept extent of the whitecap in the direction of breaking. Throughout this article we will use the notation $\Lambda(c) = \int_{-\pi}^{\pi} \Lambda(c, \theta) d\theta$, except when resolving the directional distribution of the breaking crests is required explicitly.

The mean passage rate of breaking crests past a fixed point is $c_{\text{br}}\Lambda(c_{\text{br}})dc_{\text{br}}$, where c_{br} is the propagation speed of the breaking crest, which is somewhat less than the linear phase speed c of the breaking wave (Melville and Matusov 2002; Jessup and Phadnis 2005). This will be discussed in more detail in section 4. As breaking crests propagate, they turn over a fraction of the sea surface. The fractional surface turnover rate per unit time is

$$R = \int_0^\infty c_{\text{br}}\Lambda(c_{\text{br}}) dc_{\text{br}}, \quad (3)$$

which can also be interpreted as the breaking frequency or passage rate for all scales of breaking waves at a fixed point (Phillips 1985).

The fourth and fifth moments of $\Lambda(c)$ can be related to the dynamics of wave breaking. Towed hydrofoil experiments (Duncan 1981) established the rate of energy loss per unit length of breaking crest as proportional to c^5 . Therefore, the wave energy dissipation rate owing to the breaking of waves of scale corresponding to phase speed c is

$$\varepsilon(c) = b\rho g^{-1}c^5\Lambda(c), \quad (4)$$

where b is an unknown, nondimensional proportionality factor (Phillips 1985). Since b is the only link between the energetics and the kinematics, we might anticipate that b is a breaking strength parameter whose dependence on the wave field is not yet known. At present, b is taken to be constant.

The total energy dissipation rate associated with whitecapping is

$$\dot{E} = b\rho g^{-1} \int_0^\infty c^5\Lambda(c) dc. \quad (5)$$

The associated momentum flux from breaking waves to currents is

$$\mathbf{m}(c) = b\rho g^{-1}c^4 \int_{-\pi}^{\pi} \frac{\mathbf{c}}{|\mathbf{c}|} \Lambda(c, \theta) d\theta. \quad (6)$$

Momentum from a breaking crest will be transferred mainly in the direction of the crest propagation with a smaller fraction spread laterally if the breaking crest is curved. The detailed directional momentum transfer is not yet fully understood. Here we want to evaluate the momentum flux supported by breaking waves as a function of the wind stress, and we restrict our analysis to the momentum flux component parallel to the wind direction. Thus, the total momentum flux from the wave field to currents is

$$\dot{M} \approx b\rho g^{-1} \int_0^\infty \int_{-\pi}^{\pi} \cos\theta c^4 \Lambda(c) d\theta dc, \quad (7)$$

where θ is the angle between the wave propagation and mean wind direction. Generally, different breaking scales might have different directional distributions and the directional property of the total momentum flux might have to be considered. For example, in developing wave fields and veering winds our approximation (7) would slightly underestimate the total momentum flux.

Any quantitative assessments of energy dissipation rates and momentum fluxes depend directly on the proportionality factor b , and therefore require a thorough understanding of its value and functional behavior. The original conceptual model assumes that the energy dissipation is caused by a thin whitecap propagating down the forward face of the breaking crest and opposing the underlying wave orbital motion. Here we will introduce a complementary dissipation rate model based on the mass redistribution in a breaker. Both concepts predict $b \ll 1$. This will be discussed further in section 4.

Although the theoretical framework of energy dissipation rates based on breaking crest distributions was developed two decades ago, observations of $\Lambda(c)$ in the ocean are still very limited (Ding and Farmer 1994; Phillips et al. 2001; Melville and Matusov 2002) and show a wide range of variation. We describe observations of breaking crest distributions in the open northeast Pacific at wind speeds of 10–12 m s⁻¹ and examine the implied energy dissipation rate, momentum flux, and breaking frequency. Preliminary results have been reported in Gemmrich (2005).

2. Measurement approach

Video imaging of the ocean surface spans a wide range of applications. For example, this method has been used to analyze modulations of the phase speed of short gravity waves (Gotwols and Irani 1980), small-scale surface renewal processes (Gemmrich and Hasse 1992), total whitecap coverage (Monahan and O’Muirheartaigh 1986), and characteristics of individual breakers (Melville and Matusov 2002). Recent technological developments allow for the automated processing of digital video records.

Observations of the surface wave field were taken during 24 September–10 October 2000 as part of the Fluxes, Air–Sea Interaction and Remote Sensing (FAIRS) experiment aboard Research Platform *FLIP* in the open ocean 150 km offshore of the central Californian coast (Gemmrich and Farmer 2004). Two analog black/white video cameras were mounted on R/P *FLIP*: camera 1 was located on the railing at approximately 12 m above still water level and camera 2 on the center boom at about 9-m height. The nominal field of view of camera 1 is 15.4 m \times 20.5 m and is slightly distorted due to a small camera inclination. Camera 2 is nadir looking, resulting in a 9 m \times 12 m footprint, which partially overlaps the view of camera 1. R/P *FLIP* drifted freely, orienting itself at about 15° to the wind direction. Thus, the video images are downwind and several meters to the side of *FLIP*’s hull, and are thought to represent the undisturbed wave field.

A sonic range finder, mounted on a boom next to the center boom, recorded the surface elevation at 4-Hz sampling rate (data courtesy of A. Jessup, APL UW, 2000, personal communication). The directional wave field was monitored with a set of eight 100-kHz side-scanning Doppler sonars mounted on the hull at three different depths (15, 31.5, 91.5 m) oriented in four orthogonal directions. In this way the surface values of the wave orbital motion along the sonar direction are recorded to a range of roughly 300 m. The directional wave spectrum is extracted from the sonar data using the maximum likelihood method (Trevorrow 1995).

a. Processing of video recordings

Our goal in analyzing the video recordings is to extract the length and propagation speed of actively breaking wave crests within a known surface area. As a first step, the analog video signal is converted into the digital MPEG format of 640 \times 480 pixel size (Fig. 1, top). The resulting pixel size of 3.2 \times 10⁻² m (1.9 \times 10⁻² m for camera 2) resolves even the smallest visible whitecaps without limitations.

In this study we focus on the breaking crest length, not the total whitecap area. The breaking crest length is best extracted by taking the difference between successive images. In these differential images, the forward edge of a breaking crest results in a strong positive signal, stationary features are eliminated, and the rear side of a whitecap leads to a negative signal (Fig. 1, second panel). The theoretical minimum speed that can be resolved is given by the pixel sizes times the frame rate. Thus, for the original frame rate of 30 frames per second, differential signals are limited to propagation speeds >1 m s⁻¹. Therefore, we downsample the sequence of differential images to 10 frames per second. This improves the theoretical resolvable propagation speed to >0.3 m s⁻¹, corresponding to a 1 pixel displacement. Hence, a breaker moving at 1.5 m s⁻¹ travels 5 pixels from one frame to the next. Next, the differential images are converted into binary images. This conversion is based on a threshold that is determined manually by trial and error and remains fixed. Any interconnected positive-valued pixels are considered as individual image objects. One of the advantages of analyzing differential images is that the average value of the differential images depends only marginally on the overall brightness of the raw image, thus justifying the common threshold value approach taken here. Ideally, the binary images would contain only the forward edge of breaking crests (Fig. 1, third panel). However, occasionally the tether lines and the floatation of the deployed instrumentation also remain as positive signals. The properties of these objects are rather different

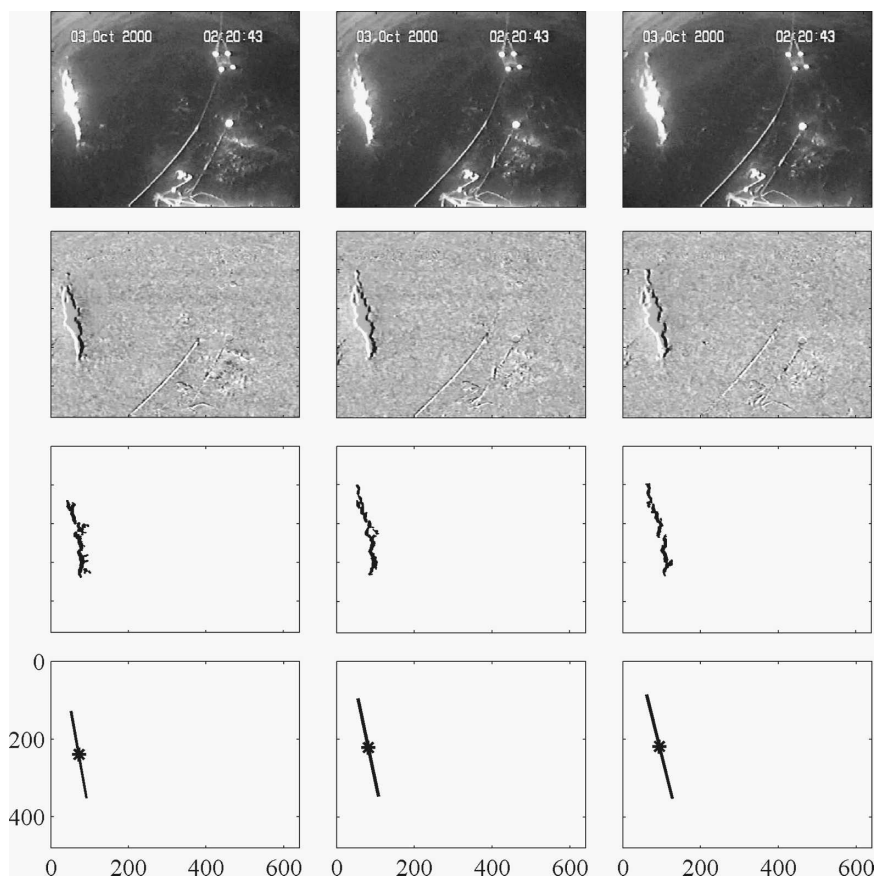


FIG. 1. Extraction of breaking crest properties: (top) sequence of video frames, (second panel) corresponding differential images, (third panel) forward edges of breaking crest based on threshold filter of differential images, and (bottom) major axis and centroid of ellipse fitted through forward crest edges. All sequences are shown at a 10-Hz frame rate.

from genuine whitecaps and these signals are removed during the subsequent analysis, as will be discussed below. In the next step, a standard Matlab image processing routine is applied to approximate each object in the binary image by an ellipse. Its centroid location (X_i, Y_i) , major and minor axis length and orientation, L_i, W_i and ϕ_i , respectively (Fig. 1, bottom), as well as the corner locations and the total area of the object are recorded onto a file. Occasionally the thresholding mechanism splits a single whitecap edge into several segments, as seen in the third image of Fig. 1 (third panel). Therefore, neighboring objects within a distance less than 20 pixels are combined into a single object if the following conditions are met: the major axis orientations of the segments are within 15° of each other and the linear fit through the centroids is aligned to within 15° with the average of the major axes orientations. If these conditions are not met, the segments are recorded as individual objects.

The task of extracting the speed and length of break-

ing crests consists of (i) tracking recorded objects across subsequent images and (ii) verifying that these objects, indeed, represent whitecaps. For each object of a starting image the corresponding object in the following image is searched for. The search is based on following criteria, which were established by trial and error and confirmed by visual cross checking for individual breaking events:

- the propagation direction is within $\pm 90^\circ$ of the wind direction
- the propagation direction is within $\pm 30^\circ$ of the minor axis orientation
- the centroid displacement is limited to $\Delta s < 1.5c_p/F_s$, where c_p is the dominant wave phase speed and F_s is the image frame rate
- the changes in object area and the major axis length are less than 25%.

If a corresponding object can be identified, it is flagged as being assigned and then the search is contin-

ued in subsequent images until the object propagates outside the image or it ceases to exist; that is, in the raw video image the contrast between the whitecap and the background is below a certain threshold or the whitecap remains stationary. Generally, whitecaps are tracked across a range of $N = 5$ to 12 images, corresponding to 0.5–1.2 s. Their displacement speed $c_i = \Delta s_i / F_s$ is estimated for each pair of successive images, where Δs_i is the displacement of the object centroid from image i to image $i + 1$.

The whitecap displacement velocity is the combination of the true whitecap propagation, that is, the nonlinear phase velocity of the breaking wave \mathbf{c}_{brk} , plus any advection owing to underlying long waves with velocity \mathbf{v}_i so that $\mathbf{c}_i = \mathbf{c}_{\text{brk}} + \mathbf{v}_i$. The advection velocity \mathbf{v}_i depends on the phase of the long wave and is highest at the long-wave crest. Its determination will be described later. Since short waves break near the crest of the long waves, the whitecap displacement speed is often largest at the beginning of the breaking. We assign the whitecap record a single whitecap displacement speed $c = c_{1/3}$, that is, the mean of the highest one-third of the speeds within the record, a duration $T = N/F_s$, a breaking crest length $L = \max(L_i)$, a mean propagation direction $\theta = \tan^{-1}[(Y_N - Y_1)/(X_N - X_1)]$, and a time of occurrence $t = t_1$. These whitecap properties are recorded to a file for further processing, including the correction for riding wave advection.

If no corresponding object can be identified in the subsequent image based on the above search criteria, the object is flagged as a nonwhitecap signal and excluded from further processing. Visual tests revealed that this scheme removed more than 90% of nonwhitecap signals, but captured all large-scale breaking waves (Fig. 1) and close to 90% of whitecaps with weaker contrast.

b. Breaker speed extraction

As stated above, the whitecap displacement is due to a combination of the propagation of the breaking crest, which occurs at the phase velocity of the breaking wave, and advection by the orbital motion of underlying longer waves. Therefore, an estimate of the long-wave orbital motion is required to extract the true phase velocity of the breaking wave.

The speed of the orbital motion at the crest of a monochromatic wave is $v = a\omega$, where a is the wave amplitude and ω the wave frequency. As described below, the advection speed owing to long waves may be estimated from a time series of the surface elevation.

The sonic range finder monitored the surface elevation within the footprint of camera 1. Here we are only concerned about the whitecap advection by long waves

and for wavelengths $\lambda > 4l$, where l is the width of the video image, the surface elevation record can be considered as representative of the entire area of the video image. To extract the long-wave properties, the surface elevation time series is decomposed into intrinsic mode functions by way of the empirical mode decomposition (Huang et al. 1998). The Hilbert transform $H(t)$ of the dominant intrinsic mode function $I(t)$ defines the local long-wave amplitude

$$a_{\text{loc}}(t) = [I^2(t) + H^2(t)]^{1/2} \quad (8)$$

and frequency

$$\omega_{\text{loc}}(t) = \frac{d}{dt} \phi(t), \quad (9)$$

where $\phi = \tan^{-1}[H(t)/I(t)]$. Thus, the long-wave orbital motion is

$$u_{\text{long}}(t) = a_{\text{loc}}\omega_{\text{loc}}. \quad (10)$$

Only whitecaps associated with breaking waves shorter than the underlying long waves are advected, not the whitecaps of breaking long waves. To automate the calculation of the advection speed without introducing artificial advection of long-wave whitecaps, the advection speed is reduced by the orbital speed u_{brk} of the breaking wave itself,

$$u_{\text{adv}}(t) = u_{\text{long}} - u_{\text{brk}}. \quad (11)$$

Approximating the ratio of the orbital speeds by the ratio of the phase speeds, it follows that

$$\langle u_{\text{adv}}(t) \rangle \simeq v = \left\langle \left(1 - \frac{c_{\text{wc}}(t)}{c_{\text{long}}(t)} \right) u_{\text{long}}(t) \right\rangle, \quad (12)$$

where $c_{\text{long}}(t) = g/\omega_{\text{loc}}(t)$ and c_{wc} is approximated by

$$c_{\text{wc}} = c_{1/3} \frac{1}{1 - \omega_{\text{loc}}^3 a_{\text{loc}} c_{1/3} g^{-2}},$$

that is, the Doppler-shifted linear dispersion relation, and the angle brackets indicate time averaging over the duration of the whitecap.

The advection speed v given by (12) is calculated for every whitecap event and a characteristic phase speed

$$c_{\text{br}} = c_{1/3} - v \cos \varphi, \quad (13)$$

where φ is the angle between the long wave and the breaking wave propagation direction, is assigned to each event. Thus, the entire whitecap is associated with a single phase speed and therefore with a single spectral wave scale.

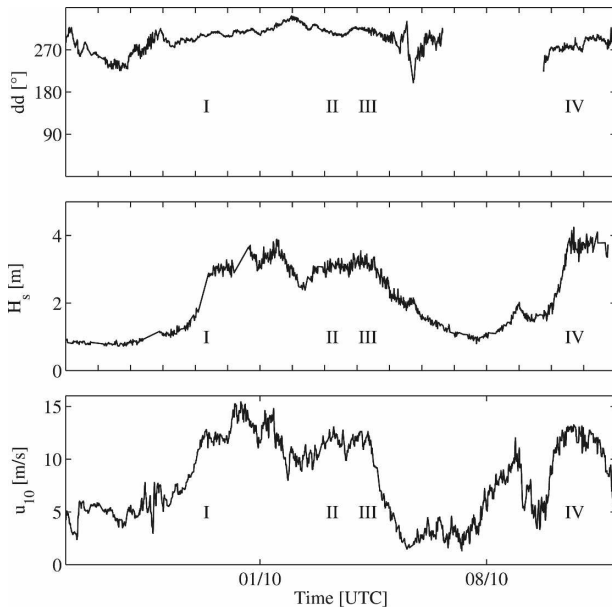


FIG. 2. Environmental conditions during the FAIRS experiment. Midpoints of individual datasets are marked by I–IV. (top) wind direction dd , (middle) significant wave height H_s and (bottom) wind speed at 10-m height u_{10} .

3. Observations

The FAIRS experiment included wind conditions ranging from almost calm up to 15 m s^{-1} . The resulting wave field ranged from pure swell conditions with significant wave height $H_s < 1 \text{ m}$ to young wind seas on top of swell with $H_s > 4 \text{ m}$. Here we report on four datasets recorded under various wind forcing and wave field conditions (Fig. 2). Significant wave height H_s and peak period T_p are based on the acoustic rangefinder data and are in good agreement with wave property estimates from data of side-scanning sonars mounted on *FLIP*'s hull. The wind stress estimates τ (provided by J. Edson, WHOI, 2000, personal communication) were obtained by the eddy correlation method.

Dataset I, 0950–1450 UTC 29 September 2000, follows a period of increasing wind speed. For several days prior to this dataset winds were very light ($< 4 \text{ m s}^{-1}$) and the wave field was dominated by swell with $H_s < 1 \text{ m}$. Approximately 11 h before the start of this dataset the wind speed u_{10} increased steadily for a period of 10 h and peaked at $u_{10} = 12.8 \text{ m s}^{-1}$. Throughout the dataset the wind speed stayed nearly constant at 12 m s^{-1} with steady direction from west-northwest, creating unlimited fetch conditions. At the beginning of the dataset the significant wave height H_s was 2.8 m and continued to rise to 3.1 m. The dominant wave period was $f_p = 0.13 \text{ Hz}$ and the wave age $c_p/u_* \approx 26$, where u_* is the friction velocity in air. This dataset represents a *developing sea*, based on the fact that the wave height

increased during this deployment and despite the relatively large wave age.

Dataset II, 0005–0230 UTC 3 October 2000, occurred after 3 days of sustained wind speed $u_{10} > 10 \text{ m s}^{-1}$, with well-developed windwaves at wave age $c_p/u_* \approx 33$, significant wave height $H_s = 3 \text{ m}$, and dominant frequency $f_p = 0.11 \text{ Hz}$. The wind speed was $u_{10} \approx 11.5 \text{ m s}^{-1}$ and wind direction from west-northwest. This dataset represents a *developed sea*.

The third dataset, 2345 UTC 3 October–0245 UTC 4 October 2000, approximates a *fully developed sea*. The dominant frequency remained unchanged at $f_p = 0.1 \text{ Hz}$, the wind speed had increased to $u_{10} \approx 12.5 \text{ m s}^{-1}$ and the significant wave height reached $H_s = 3.2 \text{ m}$. The wave age was $c_p/u_* \approx 33$. The wind direction remained west-northwest, that is, an unlimited fetch condition. For this dataset, the data coverage of camera 1 is limited to 0145–0230 UTC 4 October.

Dataset IV, 1100–1430 UTC 10 October 2000, occurred at the end of a rapid increase of wind speed from less than 5 to about 13 m s^{-1} . The wind direction stayed constant at 270° , resulting in unlimited fetch. The significant wave height increased from < 2 to $> 4 \text{ m}$. The dataset itself covers a period of slow increase in wind speed, from 11.8 to 13 m s^{-1} , but with a significant increase in wave height from $H_s = 2.5$ to $H_s = 3.9 \text{ m}$ and a reduction in dominant wave frequency from $f_p = 0.16$ to $f_p = 0.10 \text{ Hz}$. The wave age was $c_p/u_* \approx 29$. This dataset represents a growing sea superimposed upon a significant swell and will be labeled *mixed sea*. Lighting conditions were poor during this dataset, which likely results in an underestimation of small-scale breakers.

a. Scale of breaking waves

Our analysis extracts the velocity \mathbf{c}_{br} of every breaking event occurring within the video footprint. It has been suggested that due to strong nonlinear effects the phase speed c_{br} of a breaking wave is less than the phase speed c of a corresponding linear wave, $c_{br} < c$ (Melville and Matusov 2002; Jessup and Phadnis 2005). Here we take the observed phase speed of breaking waves c_{br} as a surrogate for the scale of wave breaking, and its normalization with the dominant phase speed c_{br}/c_p yields information on the spectral occurrence of wave breaking.

Wave breaking occurs over a wide range of scales (Fig. 3). However, the breaking scales cover different ranges of the wave spectrum, depending on wave development. In the developing sea case, phase speeds of breaking waves span from approximately 1/10 of the dominant phase speed (i.e., with a wavelength corresponding to 1/100 of the dominant wavelength) up to the dominant wave speed. At the other extreme, in the

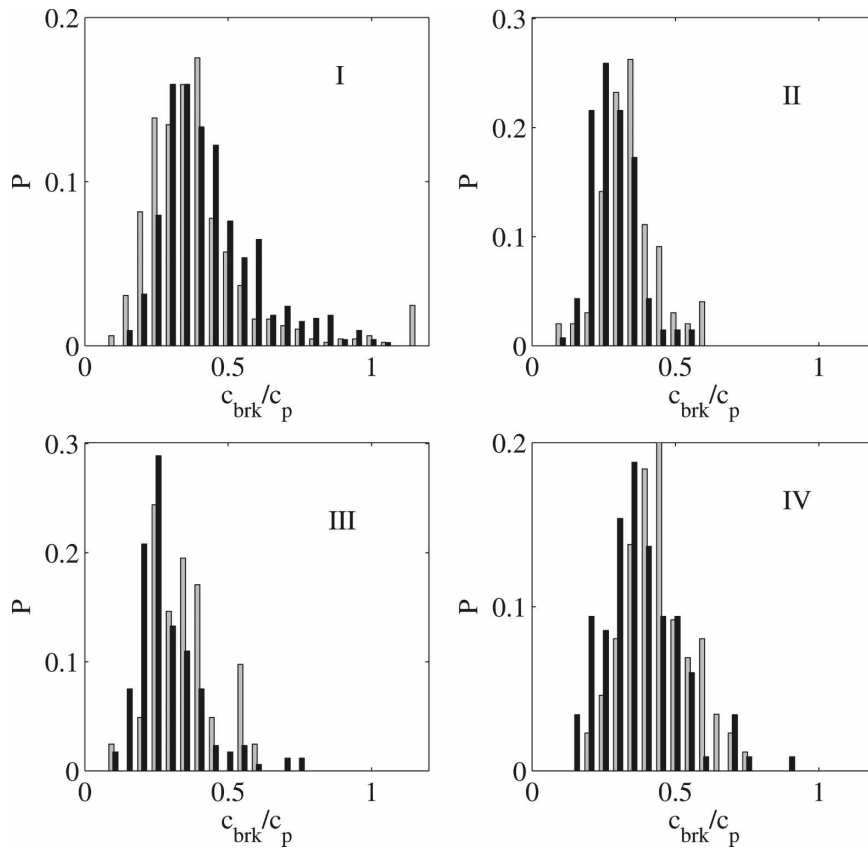


FIG. 3. Distribution of the normalized whitecap propagation speed c_{brk}/c_p as obtained from camera 1 (gray bars) and camera 2 (black bars). Individual panels correspond to the four datasets indicated in Fig. 2. The indicative mean breaker passage rate for these datasets is given in Fig. 10a.

fully developed sea we observed hardly any breaking at scales corresponding to phase speeds larger than about $0.4 c_p$. As the wave age increases, the distribution of breaking scales narrows significantly and the peak of the breaker phase speed distribution shifts from about $0.4 c_p$ to $0.2 c_p$.

For all four datasets the distributions of breaking wave phase speeds obtained from camera 2 and camera 1 (Fig. 3) are in good agreement, despite the distortion introduced by the oblique view of camera 1. The largest scales of wave breaking seem to be not fully resolved by camera 2, resulting in a cutoff of breakers with phase speed greater than approximately 14.5 m s^{-1} . However, according to camera 1 data, this cutoff affects only $<1\%$ of breaking events.

b. Breaking crest length distribution $\Lambda(c)$

For each breaking event the whitecap propagation speed c_{br} , the mean propagation direction θ_{br} , the length of the major object axis L_{br} , and the event duration t_{br} are known.

The along-crest length L_{br} of the breaking section of wave crests covers more than two orders of magnitude in our datasets, but its distribution is likely a function of the wave field directional spreading. A related, nondimensional property is the breaking aspect ratio $L_{\text{br}}/\lambda_{\text{br}}$, where $\lambda_{\text{br}} = 2\pi g^{-1}c_{\text{br}}^2$ is the wavelength associated with the breaking crest. The limited field of view of our cameras severely limits the assessment of aspect ratios of intermediate- to large-scale breakers (Fig. 4). Nevertheless, some trends may be seen in our datasets. Based on statistical arguments one can assume that those breaking crests that are only partially included in the camera field of view are, on average, twice as long as the resolved part (assuming one end is visible). Thus, aspect ratios of larger wave scales, say $c/c_p \geq 0.5$, are most likely not more than twice the directly observed values. We find that aspect ratios are generally smaller than unity, the majority being less than 0.4. Interestingly, in the developing sea most aspect ratios of short breaking waves are greater than 0.4, and thus are much larger than those of intermediate- to large-scale waves.

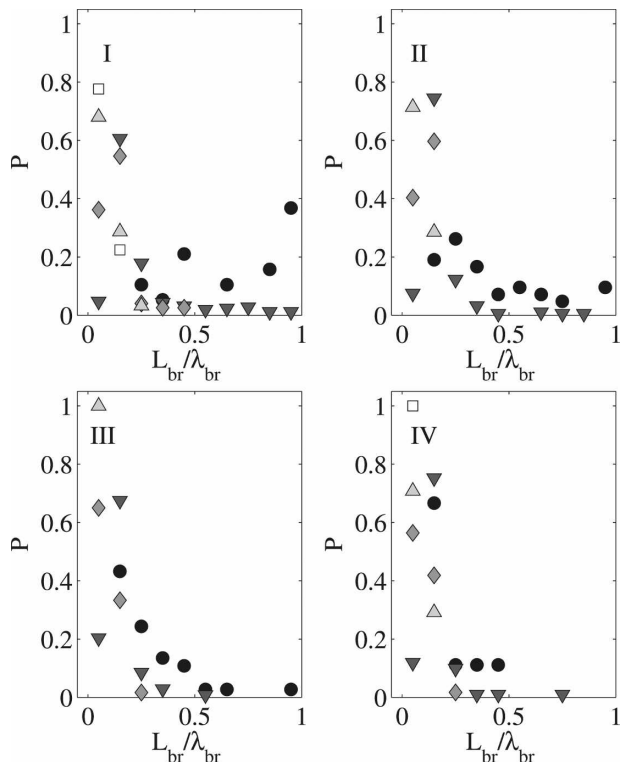


FIG. 4. Distribution of the normalized individual breaking crest length L_{br}/λ_{br} for different wave bands centered at normalized phase speed c/c_p , ranging from 0.1 (black circle), to 0.3 (black triangle-down), 0.5 (gray diamond), 0.7 (light gray triangle-up), and 0.9 (white square). Individual panels correspond to the four datasets indicated in Fig. 2. Note, intermediate- to large-scale waves are likely not fully resolved.

Again, these results are severely limited by the camera field of view and further data are required to test our preliminary findings. However, the subsequent analysis of breaking crest length distributions $\Lambda(c)$ deals with crest lengths per unit area, and this analysis is not restricted by the camera field of view.

At an arbitrary instant during the total observation time T , the expected breaking crest length of an individual event is $L_{br}t_{br}/T$. The expected breaking crest length of an event in the speed range $c, c + \Delta c$ and the range of propagation direction $\theta, \theta + \Delta\theta$ is the summation over all events within this speed range that also fall within the propagation range, $\sum L_{br}t_{br}/T$. Thus, the average length of breaking crest per unit area per unit speed interval and unit propagation direction interval is

$$\Lambda(c, \theta) = \sum L_{br}t_{br}/(T A \Delta c \Delta \theta), \tag{14}$$

where A is the area of the video footprint. The azimuthal integrated breaking crest length distribution $\Lambda(c)$ is obtained if the summation is performed over all

events within a speed range, regardless of propagation direction.

c. The dissipative scale

Phillips' (1985) concept of spectral wave breaking relates whitcapping to spectral components of the wave field. A natural wave field consists of a continuum of spectral components, and there are different ways to associate an individual whitcap with such components. Here we regard a whitcap as a single entity associated with a *single* spectral wave component, defined by the propagation speed of the centroid of the breaking crest. A similar approach is taken by Ding and Farmer (1994) who tracked the source of ambient noise associated with wave breaking events. Phillips et al. (2001) identified breaking crests in radar backscatter signals. Since their data do not include azimuthal information, the crest is essentially represented by a single point and therefore is associated with a single speed and wave component.

Recently, Jessup and Phadnis (2005) presented two methods, based on particle imaging velocimetry (PIV) algorithms, to track microscale breakers. In one case they identified breaking crests by a threshold applied to an IR image. The propagation of the crest is then tracked by PIV and the mean velocity is assigned to define the spectral component of the breaker. In the second method, breaking events are identified as regions of increased velocities and the breaker is associated with the mean speed within these regions. Although these methods differ quantitatively, they agree fundamentally in that they each associate a breaking event with a single spectral wave component.

Melville and Matusov (2002) take an entirely different approach and treat a whitcap as an aggregation of breaking crest segments of different spectral wave components. Their video data, recorded from an airplane at 450-m altitude, has a sampling rate of 5 Hz and a pixel resolution of roughly 0.5 m. Based on a brightness threshold, they identify the perimeter of a whitcap and by PIV track the velocity of each pixel of the perimeter. The mean velocity of the rearward pixels defines the whitcap advection, which is then subtracted from the velocity of the forward perimeter pixels. A running average is applied to the velocity calculations, which results in approximately 0.5-m spacing of velocity estimates along the forward edge of a whitcap. This method differs in two ways from the methods described above: (i) only actively expanding whitcaps are included in the analysis and (ii) individual whitcaps contribute to a range of different spectral wave scales, many of them corresponding to phase speeds much

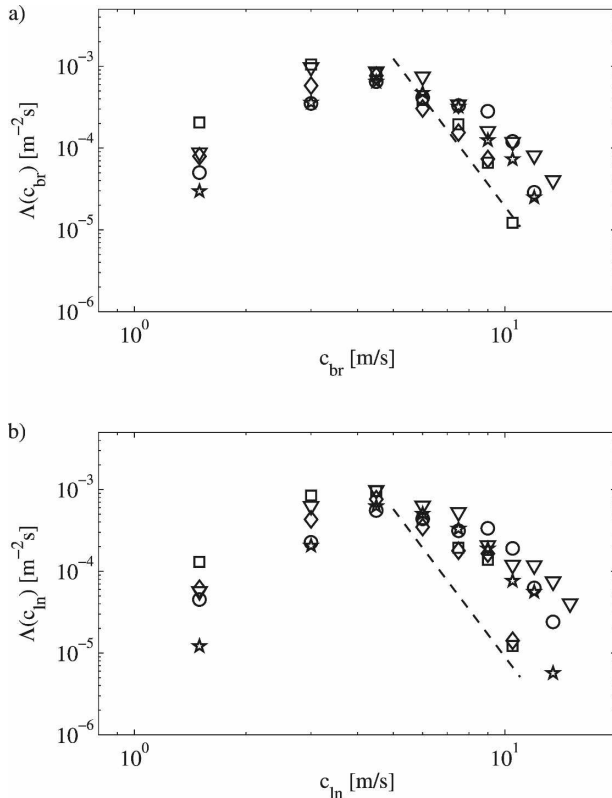


FIG. 5. (top) Breaking crest length distribution $\Lambda(c_{br})$ as function of the breaker phase speed c_{br} . The symbols (\circ , ∇ , \square , \diamond , \star) correspond to datasets Ia, Ib, II, III, and IV, respectively. The dashed line indicates a c^{-6} dependence, predicted in Phillips (1985). (bottom) Same data transformed to linear wave phase speed c_{in} . (See section 4.)

slower than the mean advancement speed of the breaking crest.

Generally, the breaking crest length of individual events increases with wave scale (Fig. 4). Therefore, the breaking crest length distribution $\Lambda(c)$ shows a slightly different behavior than the breaking occurrence rates given in Fig. 3. For the following analysis, dataset I, which occurred during a period of rapid wave field development, has been divided into two segments of equal numbers of whitecap events. The four datasets thus form five data segments.

For all five data segments, $\Lambda(c)$ peaks at intermediate wave scales with phase speeds of $3\text{--}4\text{ m s}^{-1}$, corresponding to $c/c_p \approx 0.3$ (Fig. 5). Around the peak of the $\Lambda(c)$ distribution, the values from the different data segments vary by roughly a factor 2, whereas at the smallest and the largest wave scales the different datasets spread more than one order of magnitude. Phillips (1985) predicts $\Lambda(c) \propto u_*^3$, and Melville and Matusov (2002) found that the scaling factor $(10/u_{10})^3$, where u_{10} is the 10-m-height wind speed (m s^{-1}), col-

lapsed their datasets recorded at different wind speeds (7.2 , 9.8 , and 13.6 m s^{-1}). However, in our four datasets this scaling factor varies by less than 15% and therefore does not significantly reduce the spreading between $\Lambda(c)$ values of the different datasets.

The concept of a spectral equilibrium range (Phillips 1985) assumes a balance between energy input, nonlinear energy transfer, and energy dissipation at intermediate wave scales. In this equilibrium range the wave height spectrum scales as

$$S(\omega) \propto \omega^{-4}. \quad (15)$$

Therefore, the form of the energy input

$$E_{in}(\omega) = g\beta S(\omega) \quad (16)$$

with the wave growth factor (Plant 1982)

$$\beta \propto \omega(u_w/c)^2, \quad (17)$$

where u_w is some measure of the wind speed, translates into a c^{-1} dependence of the spectral wind energy input in c space, $E_{in}(c) \propto c^{-1}$. The equilibrium concept requires the same c dependence of the spectral dissipation and, therefore, based on (4), it follows that $\Lambda(c) \propto c^{-6}$. It should be noted that the inferences made about the shape of $\Lambda(c)$ are based on the assumption that the proportionality factor b in (4) is scale independent.

At scales larger than the peak of the observed $\Lambda(c)$ distribution, $\Lambda(c)$ indeed falls off approximately as c^{-6} , consistent with the equilibrium range concept. However, the drop-off of $\Lambda(c)$ values at wave scales corresponding to $c \leq 4\text{ m s}^{-1}$ is somewhat unexpected. To test whether the shape of the $\Lambda(c)$ curve could be caused by systematic biases introduced in the processing scheme, the limitations of its spatial and temporal resolutions are estimated. The phase speeds of the two lowest bins in Fig. 5 are $c = 1.5$ and $c = 3\text{ m s}^{-1}$, corresponding to wavelengths $\lambda = 1.4$ and 5.8 m and wave periods $\tau = 1$ and 2 s . Assuming that the duration of the breaking process is longer than 0.5τ and the breaking crest length L is 0.7 times the downwind extension of the breaking patch (Phillips et al. 2001) yields $L > 0.3\lambda$. That means even for the smallest breaker scales resolved we expect a breaking crest length $L > 0.5\text{ m}$, which is easily detected by the video resolution. However, the processing scheme requires a sequence of at least four images to estimate the object propagation speed. The sampling of the differential images is 10 Hz ; that is, only breaking events of duration $t_{br} \geq 0.4\text{ s}$ are resolved. This limitation might reject some of the smallest breakers as it requires $t_{br} \geq 0.4\tau$. At the largest breaker-scale bin with $c = 13.5\text{ m s}^{-1}$, the duration threshold yields a centroid propagation dis-

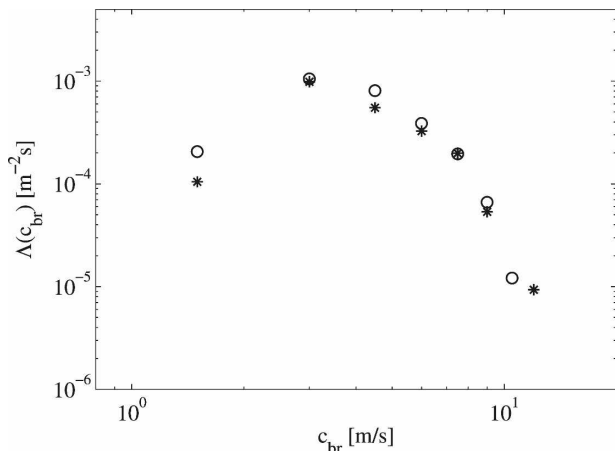


FIG. 6. Breaking crest length distribution $\Lambda(c_{br})$ as function of the breaker speed c_{br} for dataset II. Sampling rates of differential video frames are 10 Hz (open circle) and 15 Hz (asterisks).

tance of 5.4 m, which is equivalent to 60% of the downwind extent of the video image. Thus, breakers with $c = 13.5 \text{ m s}^{-1}$ originating closer than 5.4 m to the downwind edge of the video image will be rejected by the automated processing.

To test the severity of these limitations we processed dataset II at the full differential images sampling rate of 15 Hz. The $\Lambda(c)$ values obtained at the two different sampling rates show the same functional behavior (Fig. 6). Small differences between the two cases give an indication of the accuracy of the processing scheme. The low $\Lambda(c)$ values at small wave scales cannot be attributed to the video sampling rate. Small-scale breakers are associated with less air entrainment than larger breakers, and it is possible that the visible contrast of some small-scale breakers is not sufficient to be picked up by the automated processing, thus underestimating the breaking crest length in the lower velocity bins.

During the course of the experiment, the wind direction varied only slightly (Fig. 2). Furthermore, in all four datasets swell and wind waves were aligned within 30° , producing nearly unidirectional wave fields. This is also reflected in the directional distribution of the breaking crest length (Fig. 7). Here we present data in the nondimensional form $c_p^2 g^{-1} \Lambda(c/c_p, \theta)$, that is, the breaking crest length normalized by the dominant wave scale k_p^{-1} (where k_p is the dominant wavenumber) as a function of the breaker phase speed normalized by the dominant phase speed. Again, dominant breakers occur only in the younger sea cases (I, IV), whereas in the developed wave fields little breaking is associated with wave scales corresponding to $c/c_p \geq 0.6$.

The camera orientations are only known within

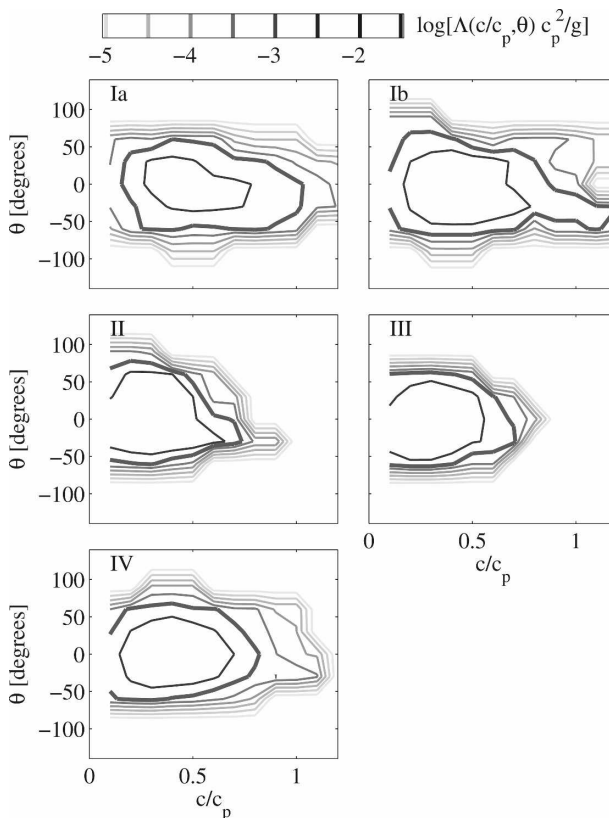


FIG. 7. Nondimensional breaker length distribution $c_p^2 g^{-1} \Lambda$ as a function of the propagation direction θ and the normalized linear phase speed of breaking waves c_{in}/c_p as obtained from the four datasets indicated in Fig. 2. The contour spacing is 0.5 and the thick contour line corresponds to -2 .

about 15° . Therefore, for the individual datasets the whitecap propagation direction is rotated to a zero median direction, which can be assumed to be the mean wind direction. In terms of directional distribution we do not see any significant differences between the four data sets (Fig. 7). Breaking waves occupy the entire range of positive downwind directions $-90^\circ < \theta < 90^\circ$, particularly at short to intermediate wave scales ($c/c_p \leq 0.5$). However, the weighted spreading width $[\int_{-\pi}^{\pi} \theta^2 \Lambda(c/c_p, \theta) d\theta / \int_{-\pi}^{\pi} \Lambda(c/c_p, \theta) d\theta]^{1/2}$ is much narrower, about 30° , and does not vary significantly with wave scale. This is roughly consistent with Phillip’s (1985) expectation that “a preponderance of breaking-wave events advance in a direction close to that of the wind.”

4. Discussion

The first, fourth, and fifth moments of the breaking length distribution provide information on the kinematics and dynamics of breaking waves. However, only breaking events exceeding a certain visible brightness contrast due to air bubbles are included in the following

analysis. This excludes weaker, small-scale breakers with, say, $c < 1 \text{ m s}^{-1}$, as well as microscale breakers.

The observations yield the breaker speed c_{br} (corrected for the long-wave Doppler shift) and the associated breaking crest length distribution $\Lambda(c_{\text{br}})$. However, the usual spectral wave description, as applied in spectral wave models, is expressed in terms of the linear Fourier mode speed c_{ln} (or the equivalent frequency or wavenumber given by the linear wave dispersion relation), and the fourth and fifth moments of $\Lambda(c_{\text{ln}})$ are the required quantities. Assuming that

$$c_{\text{ln}} = \alpha^{-1} c_{\text{br}}, \quad (18)$$

this transformation is straightforward. Further, it is easily seen that the energy and momentum fluxes transform consistently, if they are based on c_{ln} , but this no longer holds if they are based on c_{br} .

The breaker speed c_{br} is somewhat less than the linear phase speed of the breaking wave c_{ln} . Here we take $\alpha = 0.9$, based on wave tank results (Banner and Peirson 2007), which is a slightly weaker reduction than $\alpha = 0.8$ assumed in Melville and Matusov (2002).

The basis of the transformation is the fact that the total breaking crest length is invariant so that

$$\Lambda(c_{\text{ln}}) dc_{\text{ln}} = \Lambda(c_{\text{br}}) dc_{\text{br}}, \quad (19)$$

yielding

$$\Lambda(c_{\text{ln}}) = \alpha \Lambda(c_{\text{br}}). \quad (20)$$

In the following, we present energy dissipation rates and momentum fluxes in the linear phase speed space, and for brevity write $c_{\text{ln}} = c$. For completeness, Fig. 5b shows $\Lambda(c_{\text{ln}})$. However, the overall breaking rate R at a fixed location, given by the first moment of the breaking crest distribution, is only defined in terms of the breaking crest propagation speed, that is,

$$R_{\Lambda} = \int c_{\text{br}} \Lambda(c_{\text{br}}) dc_{\text{br}}, \quad (21)$$

and $R = R_{\Lambda}$ will be calculated accordingly.

a. Total breaking rate

The breaking rate R at a fixed location is equivalent to the fractional surface area turnover rate at an arbitrary time. Thus, R is an important quantity for air–sea exchange processes, for example, relevant for specifying surface renewal and bubble entrainment in air–sea gas flux models. In the framework of breaking crest length distribution, the breaking rate is a direct quantity, independent of empirical constants. Therefore, R can provide a consistency check for the observed $\Lambda(c)$ distributions.

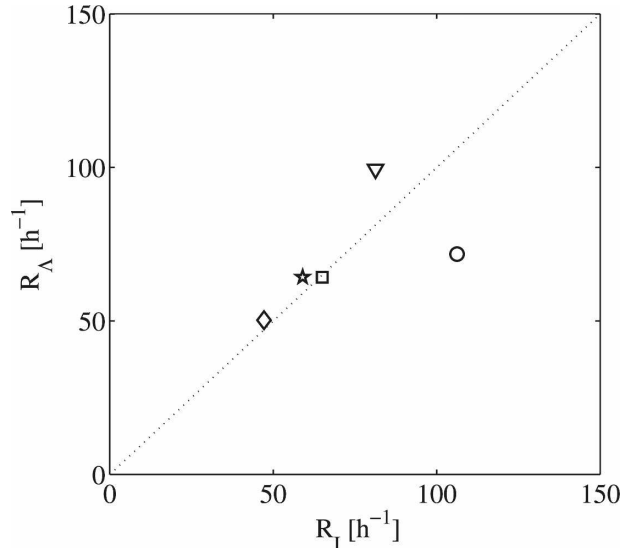


FIG. 8. Breaking rate R_{Λ} , calculated from breaking crest length distributions, compared to breaking rate R_T , estimated from the passage rate of bright targets passing a fixed spot in the video frame: symbols as in Fig. 5.

The breaking rate R ranges between roughly 50 and 120 breaking events per hour (Fig. 8). Previous observations by various investigators using a wide range of observational techniques (for a summary, see Gemmrich and Farmer 1999) report breaking rates $R \approx 0.1/\tau_p$ to $0.8/\tau_p$, where τ_p is the dominant wave period. For open ocean conditions these rates relate to the same range of values as observed in this study. The video images provide an independent estimate of the breaking rate R_T . In an automated but somewhat crude scheme, we calculate the mean brightness of a fixed spot of 10×5 pixels. If the mean brightness exceeds a certain threshold, which is determined by the overall image brightness, a breaking event is registered. We find reasonable agreement between the breaking rates based on the breaking crest distributions R_{Λ} and R_T from the video recordings (Fig. 8).

On the other hand, breaking rates inferred from breaking crest length distributions reported in Melville and Matusov (2002) are $R \approx 2 \text{ h}^{-1}$ and $R \approx 6 \text{ h}^{-1}$ for $u_{10} = 9.8$ and 13.6 m s^{-1} , respectively. These breaking rates are very low compared to previous observations under similar conditions and are likely linked to the limited video resolution and the elemental whitecap analysis applied in their study.

The breaking rate also provides insight to what conditions are favorable to wave breaking. Banner et al. (2002) found the breaking rate at specific scales to depend on the normalized wave saturation $\sigma(\omega)$, defined in (2), for the corresponding frequency band. This in-

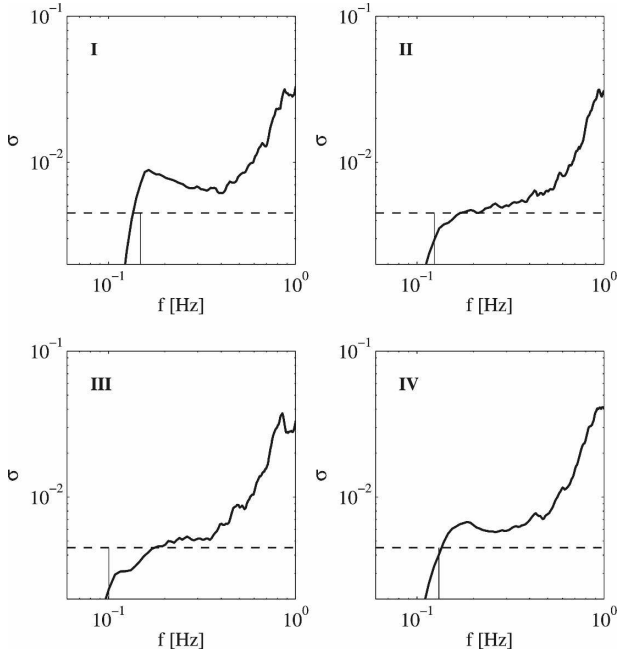


FIG. 9. Normalized wave saturation σ [defined in (2)] as function of frequency f (datasets as indicated in top-left corner). The dashed horizontal line represents the threshold for onset of breaking as determined in Banner et al. (2002); the vertical line depicts the dominant wave frequency.

direct breaking criterion is also verified by our current data. Saturation levels during datasets II and III are lower than for the two other datasets. Moreover, at lower frequencies, corresponding to waves with $c/c_p > 0.6$, the saturation in II and III is below the threshold level (Fig. 9) and no breaking occurred at these wave scales (Fig. 3). For the angular spreading $D(\omega)$ we chose an empirical expression that closely follows Hwang et al. (2000), but levels off at small wave scales. We chose $D = 0.3$ for $\omega/\omega_p \leq 1$ and $D = 0.8$ for $\omega/\omega_p \geq 3.5$ with a fifth-order polynomial matching in between.

Here we are concerned with the overall breaking rate R , which includes contributions from all spectral wave scales. Therefore, we define the mean saturation level

$$\sigma_b = \left\langle \frac{\omega^5 S(\omega)}{2g^2 D(\omega)} \right\rangle, \quad (22)$$

where angle brackets represent the average over the bandwidth $\omega_p \leq \omega \leq 5\omega_p$ and the duration of the dataset.

We find the breaking rate R to depend roughly linearly on the mean saturation level σ_b , with higher saturation levels leading to more frequent breaking (Fig. 10a). Extrapolation of our data yields $\sigma_b \approx 4 \times 10^{-3}$ as a threshold for the onset of breaking; however, the

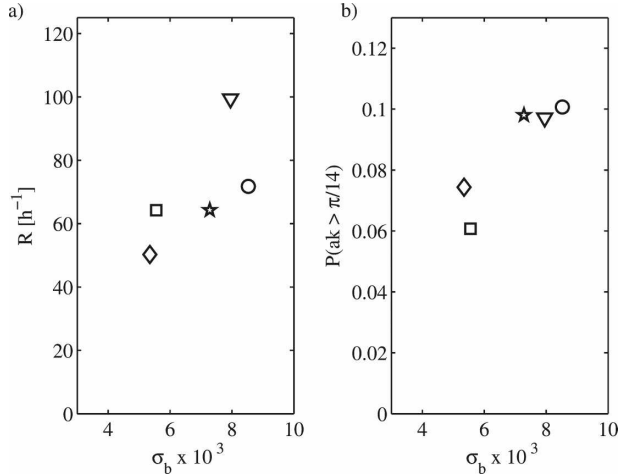


FIG. 10. (a) Breaking rate R as function of mean normalized saturation level σ_b within the band $1 \leq \omega/\omega_p \leq 5$. (b) Fraction of wave crests with steepness $ak > \pi/14$ vs mean normalized saturation level σ_b ; symbols as in Fig. 5.

band-averaged saturation, and therefore this threshold value, depends on the chosen bandwidth. Our choice of $\omega_p \leq \omega \leq 5\omega_p$ yields a threshold in good agreement with the threshold behavior of spectral breaking rates reported in Banner et al. (2002). The good agreement in magnitude and functional dependency of breaking rates inferred from the breaking crest length distributions and various different and independent observation techniques is encouraging in suggesting that our analysis captures the majority of whitecap events.

Gemmrich (2005) reports a close-to-linear relation between breaking rates and the fraction $P(ak > \chi)$ of wave crests exceeding a certain steepness threshold χ . It turns out that P is a surrogate for the saturation level (Fig. 10b), and it is preferable to relate wave breaking to the dynamically relevant saturation level σ_b rather than the indirect threshold-dependent quantity P .

b. Momentum flux and energy dissipation rate

At moderate to high wind speeds the air–sea momentum flux $\tau_a = \rho u_*^2$ is dominated by the form drag of the waves τ_w . A smaller fraction of the momentum transfer is supported by the tangential stress τ_s . The largest fraction τ_{wc} of the wave momentum is transferred locally via wave breaking to the mean currents and the remaining fraction τ_{wg} to the growing wave field,

$$\tau_a = \tau_w + \tau_s = \tau_{wc} + \tau_{wg} + \tau_s. \quad (23)$$

Thus, the local momentum flux from the waves to currents is

$$\tau_{wc} = \tilde{\gamma} \tau_a, \quad (24)$$

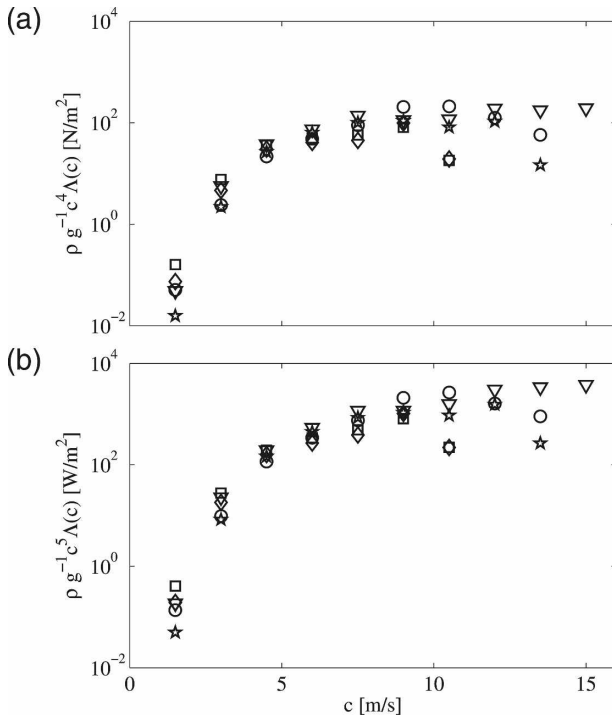


FIG. 11. Moments of $\Lambda(c)$ as function of the linear breaking wave phase speed c . Multiplied by the factor b [Eqs. (3), (5)], these data points correspond to the (top) breaking wave-induced momentum flux and (bottom) breaking wave-induced energy dissipation rate: symbols as in Fig. 5.

where the parameter $\tilde{\gamma} < 1$ depends on wind speed and wave field development (Donelan 1979). However, the spectral distribution of the wave momentum flux is not well understood. Similarly, the energy transferred from the wind to the wave field is

$$E_{in} = c_{eff} \tau_w \approx \rho c_{eff} u_*^2, \quad (25)$$

where c_{eff} is the effective phase speed of waves acquiring energy from the wind, assuming that the energy flux divergence is small (Gemmrich et al. 1994).

Spectrally resolved momentum fluxes and energy dissipation rates are inferred from the fourth and fifth moments of $\Lambda(c)$, respectively (6), (4). However, the transfer function includes the unknown proportionality factor b , and we present momentum and energy fluxes without the factor b (Fig. 11). In all five data segments the momentum flux due to breaking waves is strongest at wave scales corresponding to phase speeds of about 6–9 m s⁻¹. At wave scales with $c < 5$ m s⁻¹ the momentum flux supported by whitecapping waves falls off by roughly three orders of magnitude. Large-scale breaking events are more sparse, and therefore the momentum flux supported by larger wave scales fluctuates

considerably between the four datasets. Energy dissipation rates due to whitecapping are even more dominated by larger wave scales. The spectral distributions of the energy dissipation rates peak at $c = 8$ to 10 m s⁻¹.

The ratio of the total energy dissipation rate (5) and the integrated momentum flux (7) defines the effective phase speed of waves transferring energy from the wind to the ocean via whitecapping:

$$c_{eff} = \frac{\int_{c_g}^{c_2} c^5 \Lambda(c) dc}{\int_{c_g}^{c_2} \int_{-\pi}^{\pi} \cos \theta c^4 \Lambda(c) d\theta dc}, \quad (26)$$

where the integration spans the range from the minimum phase speed of gravity waves $c_g = 0.23$ m s⁻¹ to the largest breakers with, say, $c_2 = 15$ m s⁻¹. As discussed above, breaking-wave-related energy dissipation rates and momentum fluxes are dominated by larger wave scales. In contrast, it has been argued that waves from centimeter to meter wavelengths support a dominant fraction of the aerodynamic wave form drag at moderate to high wind speeds (Makin et al. 1995). Our video analysis is restricted to waves generating visible whitecaps, and (26) can only be evaluated for a lower integration bound of $c_1 = 1.5$ m s⁻¹ rather than $c_1 = c_g = 0.23$ m s⁻¹. This fractional integral yields a modified effective phase speed \tilde{c}_{eff} , with $\tilde{c}_{eff} > c_{eff}$, and we rely on additional assumptions to estimate the complete energy dissipation rate and air–sea momentum flux.

Budget ratios of the total energy dissipation rate in the surface layer and the total momentum flux in the atmospheric boundary layer yield $c_{eff} = O(1$ m s⁻¹) (Gemmrich et al. 1994). Terray et al. (1996) analyzed a variety of field observations of direct turbulence measurements and presented the effective phase speed, normalized by the dominant phase speed, as a function of wave age. Applying their results to our datasets results in $c_{eff} = (0.06$ to $0.17) c_p$ (Fig. 12), corresponding to $c_{eff} \approx 1$ to 2 m s⁻¹. Based on the theoretical functional form $\Lambda(c) \propto c^{-6}$, the effective phase speed is $c_{eff} = 0.95$ m s⁻¹.

The energy input into the water column via skin friction scales as $E_{skin} \propto u_*^3$. Thus, the ratio c_{eff}/u_* describes the enhancement of energy input due to waves. As the wave field develops, this ratio increases initially. However, for more mature seas the reduction of the spectral peak enhancement causes c_{eff}/u_* to slowly decrease with wave age (Terray et al. 1996) which is also seen in our data (Fig. 12b).

Both quantities \tilde{c}_{eff} and c_{eff} represent the ratios of

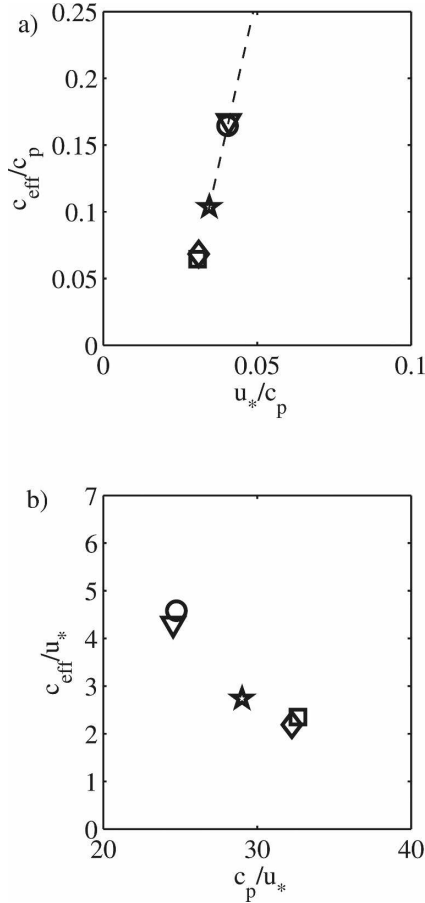


FIG. 12. The effective phase speed c_{eff} related to the energy input from wind to waves (Gemmrich et al. 1994). (top) Effective phase speed normalized by dominant phase speed, as function of inverse wave age. Data points are matched to the result of Terray et al. (1996), depicted by the dashed line. (bottom) Effective phase speed normalized by friction velocity as function of wave age: symbols as in Fig. 5.

total energy dissipation rate and total momentum flux supported by a certain wave band; in the case of \tilde{c}_{eff} only wave scales associated with whitecaps are included, whereas c_{eff} includes momentum and energy transfer by the entire capillary-gravity wave band. Thus, the difference between \tilde{c}_{eff} and c_{eff} helps to address the role of small-scale breaking waves without visible air entrainment.

Compensating for the limited wave band resolution, the effective phase speed may be estimated as

$$c_{\text{eff}} = \frac{\int_{c_1}^{c_2} c^5 \Lambda(c) dc}{\gamma^{-1} \int_{c_1}^{c_2} \int_{-\pi}^{\pi} \cos \theta c^4 \Lambda(c) d\theta dc}, \quad (27)$$

where γ represents the fraction of air-sea momentum supported by waves within a given wavenumber band and thus depends on c_1 and c_2 .

A first estimate of γ is obtained from model results, estimating the cumulative spectrum of wave-induced stress per wave band (Kudryavtsev et al. 1999), combined with an estimate of the partitioning factor $\tilde{\gamma}$ [defined in (24)]. Assuming fully developed seas, 10 m s^{-1} wind speed, and $\tilde{\gamma} = 0.85$ (Banner and Peirson 1998), the model predicts that nearly 30% of the total air-sea momentum flux is supported by wave scales corresponding to $c \geq 1.5 \text{ m s}^{-1}$. However, it is likely that γ depends on wave development and wind speed.

Estimating the partitioning factor γ from our data,

$$\gamma = \frac{c_{\text{eff}} \int_{c_1}^{c_2} \int_{-\pi}^{\pi} \cos \theta c^4 \Lambda(c) d\theta dc}{\int_{c_1}^{c_2} c^5 \Lambda(c) dc}, \quad (28)$$

requires prescribing the effective phase speeds c_{eff} . Here we take c_{eff} from the fit to the Terray et al. (1996) result according to the wave ages applicable to our datasets (Fig. 12a). Based on these assumptions, the portion of air-sea momentum flux supported by the resolved breaking waves ranges from 17% in the developing wave field to 11% in the mature sea.

c. Proportionality factor b

Equating the energy and momentum fluxes to moments of the breaking crest length distribution $\Lambda(c) dc$ is based on a simple conceptual model of a whitecap sliding down the forward face of the wave (Duncan 1981; Phillips 1985). The breaker zone on the forward face of the crest covers a fixed fraction of the wave amplitude. Assuming the breaking waves are self-similar, the cross-sectional area A_w of the breaking zone, normal to the wave crest, is proportional to the square of the wave scale $k^{-1} (= \lambda/2\pi)$, so that $A_w \propto k^{-2} = (c^2 g^{-1})^2$. The weight of this breaking zone $A_w \rho_f g$, where ρ_f is the density of the foam, exerts a tangential force $\propto c^4 g^{-1}$ per unit width of the breaker, which acts against the orbital motion u_{orb} . On the forward face of the wave the orbital motion is directed upslope and $u_{\text{orb}} \propto c$. Thus, the rate of energy loss is proportional to $\rho g^{-1} c^5$, where the proportionality factor incorporates (i) the ratio of the foam cross section and the squared wave scale, (ii) the cosine of the wave slope, (iii) the ratio of the foam density ρ_f to water density, and (iv) the ratio of the orbital velocity to the phase speed of the wave; that is,

$$b_1 = A_w k^2 \cos(ak) \frac{\rho_f u_{\text{orb}}}{\rho c}. \quad (29)$$

A second, very simple, model (Phillips et al. 2001) describes the breaking event as a jet of water being ejected forward from the wave crest. The speed u_j of the jet is about the phase speed $u_j \approx c$ and its vertical thickness $\delta \ll k^{-1}$. Thus, the energy flux per unit crest length is $\rho \delta u_j^3 / 2 \approx \rho \delta c^3 / 2 \propto \rho c^5 g^{-1}$. A shortcoming of this model is that it ignores the effect of the jet impacting the water surface. The proportionality factor includes the ratio of the jet speed to the phase speed, to the third power, and the ratio of the jet thickness to the wave scale,

$$b_2 = \frac{1}{2} \left(\frac{u_j}{c} \right)^3 \delta k. \quad (30)$$

Both models predict the proportionality factor b to be small. However, it is difficult to estimate on theoretical or empirical grounds the range of values as well as potential dependencies.

Here we propose a third conceptual model based on a breaking event as redistribution of water from the crest toward the trough region. We assume that a water parcel of cross-sectional area A_w (viewed in along-crest direction) plunges down a distance D . Then, the loss of energy from the wave, per unit crest length, is gDA_w . The time required for the redistribution is $t = (2D/g)^{1/2}$, and the rate of energy loss is thus $\varepsilon = 2^{-1/2} g^{3/2} D^{1/2} A_w$. Assuming that the length scales involved are proportional to the wave scale k^{-1} , the energy dissipation rate is given by $\varepsilon = b_3 g^{-1} c^5$, where the proportionality factor depends on the ratios of the length scales of the redistributed water parcel as well as its vertical displacement to the wave scale,

$$b_3 = (kD)^{3/2} k^2 A_w. \quad (31)$$

Both fractions are small and most likely depend on the strength of the breaking event; therefore, b_3 will be small.

In all three models, it is assumed that in nature the physical process of dissipating energy spans the same time as the active breaking of a wave crest is occurring. All three concepts confirm that the energy dissipation rate scales to the fifth power of the wave speed and predict the proportionality factor b to be small. Most likely, this value is not a constant. Dimensional analysis only requires a nondimensional proportionality factor. However, all of the models described here suggest that b may depend on the wave geometry, say $b = b(\sigma_b)$. In recent wave tank experiments the value of b varied by an order of magnitude depending on the breaker strength, with the lowest b values found for the weakest breaking (Banner and Peirson 2007).

The numerical value of b is crucial for any quantita-

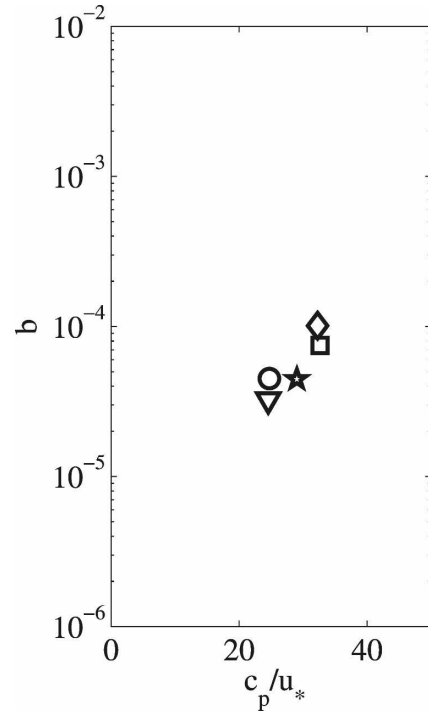


FIG. 13. Proportionality factor b as a function of wave age c_p/u_* ; symbols as in Fig. 5.

tive estimates of wave energy dissipation or wave-current momentum transfer, but it is very uncertain, with reported values applicable to the ocean ranging from $b \approx 10^{-3}$ (Phillips et al. 2001) to $b \approx 10^{-2}$ (Melville and Matusov 2002) and assumed to be scale independent.

The proportionality factor b may be estimated from the momentum flux balance (7) or the energy balance (5),

$$b = \frac{\gamma \tau_w}{\rho g^{-1} \int_{c_1}^{c_2} \int_{-\pi}^{\pi} \cos \theta c^4 \Lambda(c) d\theta dc}, \quad (32)$$

and

$$b = \frac{c_{\text{eff}} \tau_a}{\rho g^{-1} \int_{c_1}^{c_2} c^5 \Lambda(c) dc}. \quad (33)$$

From the definition of γ , these estimates are identical, yielding $3.2 \times 10^{-5} \leq b \leq 10.1 \times 10^{-5}$ (Fig. 13). Thus, in our four datasets b varies by a factor of 3 and is one to two orders of magnitude smaller than previous estimates (Phillips et al. 2001; Melville and Matusov 2002). Surprisingly, the apparent dependence of b on the wave development, expressed as wave age c_p/u_* (Fig. 13) is opposite to our initial expectations; b increases with wave age. For the five data segments, the

airside momentum flux τ_a varied only by 12% (Fig. 2). Thus, variations in b are mainly due to differences in the breaking crest length distributions. However, uncertainties in the empirical values of c_{eff} (Terray et al. 1996) and γ may also play a significant role in this counterintuitive dependence of b on the wave development.

The energy transferred from the wind to the wave field (25) is expected to be roughly twice as large in dataset I as in II (Fig. 12). However, the integrated fifth moments of the breaking crest distribution $L_5 = \int c^5 \Lambda(c) dc$ show a ratio close to 6:1, resulting in the about three times larger b values for dataset II. The differences in L_5 between datasets are due largely to the presence of dominant breakers in the younger sea states. These large-scale breakers are significantly less frequent than intermediate-scale breakers and their statistics are less robust. The L_5 values are also affected by the bandwidth Δc and the video footprint. However, erroneous rejection or inclusion of breaking events modifies L_5 only at a roughly linear dependence; that is, a hypothetical identical value of b for datasets I and II would imply that two-thirds of the large-scale breakers ($c \geq 9 \text{ m s}^{-1}$) in dataset I are processing artifacts. Similarly, erroneous classification of 10% of all events into the next higher speed band would increase L_5 by less than 7%. Therefore, we conclude that the observed trend of increasing b values with increasing wave development cannot be attributed to the uncertainties in the observed breaking crest length distributions. We take the difference of $\Lambda(c)$ from the full sampling rate and subsampled differential imagery (Fig. 6) as an indication of the estimate of these uncertainties. The resultant uncertainty in L_5 is 6%. Nevertheless, the apparent wave-development dependence of b remains puzzling and counter to the trend from wave tank experiments. This warrants further study. Based on our results here, we suggest that for open ocean conditions $b = (7 \pm 3) \times 10^{-5}$.

5. Conclusions

Close range video recording of the ocean surface was used to estimate the along-crest dimension and propagation speed of whitecaps. From these open ocean data, at four different wave development stages, the breaking crest length distribution $\Lambda(c)$ has been calculated. An important result is the specification of breaker scales in these different conditions. In fully developed sea states ($c_p/u_* = 33$) only intermediate- to small-scale breaking waves, corresponding to $c/c_p \lesssim 0, 6$, are observed. On the other hand, in developing seas ($c_p/u_* = 26$), all wave scales, including the dominant waves, are part of the breaking spectrum. This has important implications

for the shape of the energy dissipation term S_{dis} used in spectral wave models. The occurrence of wave breaking at a particular scale is linked to the wave saturation. In a previous study (Banner et al. 2002), it was found that the onset of breaking is linked to the wave saturation, normalized by the directional spreading of the wave energy. Breaking occurred only for cases with normalized wave saturation larger than 4.5×10^{-3} . This threshold behavior has been confirmed in this study. Also, the mean wave saturation within the frequency band $\omega_p \leq \omega \leq 5\omega_p$ is a good indicator for the breaker passage rate at a fixed location. The breaker passage rate obtained from the first moment of $\Lambda(c)$ indicated 50 to 100 breakers per hour, in close agreement with independent observations. This provides strong validation for the observed breaking crest length distributions $\Lambda(c)$.

The fourth and fifth moment of $\Lambda(c)$ are linked to the momentum flux from the waves to currents and the wave-induced energy dissipation rate, respectively. These fluxes are dominated by intermediate-scale waves and no indication is found of a Kolmogorov-type energy cascade in the wave field, where energy dissipation would be dominated by small-scale breakers. We find the proportionality factor $b = (7 \pm 3) \times 10^{-5}$, which is required for a quantitative assessment of wave energy dissipation rate based on breaking crest length distributions. This is much smaller than previously reported (Phillips et al. 2001; Melville and Matusov 2002). In a conceptual model, describing wave breaking as displacement of water parcels from the crest into the trough region, we offer a heuristic explanation why we expect b to vary depending on the wave state. However, a detailed study of the functional dependence of the proportionality factor b is still crucial before implementing breaking crest length distributions into wave energy dissipation functions.

In the case of developed wave fields and 12 m s^{-1} wind speed, about 11% of the air–sea momentum flux is supported by air-entraining breaking waves. This fraction increases for younger seas.

The Duncan–Phillips concept of estimating wave kinematics and dynamics from breaking crest length distribution was introduced more than two decades ago. Advances in video technology and computational image processing have opened this concept to relatively easy field observations. We expect that an increase in such observational data, covering various wave field conditions, will help to solve the remaining open issues, in particular the functional dependence of the proportionality factor b . Furthermore, this study is based only on wave breaking that generated visible air entrain-

ment, and we recommend that future studies also include smaller-scale breaking waves and microbreakers.

Acknowledgments. This work was made possible with the funding by the Canadian Foundation for Atmospheric and Climate Sciences (CFCAS). Data collection was part of the FAIRS project, supported by the Office of Naval Research. We are indebted to the crew of R/P *FLIP* and the technical staff of the acoustical oceanography group at the Institute of Ocean Sciences (Sidney, BC). A. Jessup (APL-UW) and J. Edson (WHOI) provided supplementary data. MLB also gratefully acknowledges support during this investigation from the U.S. Office of Naval Research under the CBLAST Departmental Research Initiative. Part of the analysis was done during one author's (JG) visit to the Institute for Baltic Sea Research Warnemünde, and the hospitality and many insightful discussions with H. Burckhard and L. Umlauf are greatly acknowledged. The critical reviews by two anonymous reviewers helped to improve the manuscript.

REFERENCES

- Ardhuin, F., A. D. Jenkins, D. Hauser, A. Reniers, and B. Chapron, 2005: Waves and operational oceanography: Towards a coherent description of the upper ocean for applications. *Eos, Trans. Amer. Geophys. Union*, **86**, 37–39.
- Banner, M. L., and W. L. Peirson, 1998: Tangential stress beneath wind-driven air-water interfaces. *J. Fluid Mech.*, **364**, 115–145.
- , and —, 2007: Wave breaking onset and strength for two-dimensional deep water wave groups. *J. Fluid Mech.*, **585**, 93–115.
- , J. R. Gemmrich, and D. M. Farmer, 2002: Multiscale measurements of ocean wave breaking probability. *J. Phys. Oceanogr.*, **32**, 3364–3375.
- Ding, L., and D. M. Farmer, 1994: Observations of breaking surface wave statistics. *J. Phys. Oceanogr.*, **24**, 1368–1387.
- Donelan, M., 1979: On the fraction of wind momentum retained by waves. *Marine Forecasting*, J. C. J. Nihoul, Ed., Oceanography Series, Vol. 25, Elsevier, 141–159.
- Duncan, J. D., 1981: An experimental investigation of breaking waves produced by an airfoil. *Proc. Roy. Soc. London*, **377A**, 331–348.
- , 2001: Spilling breakers. *Annu. Rev. Fluid Mech.*, **33**, 517–547.
- Gemmrich, J., 2005: On the occurrence of wave breaking. *Rogue Waves: Proc. 'Aha Huliko'a Hawaiian Winter Workshop*, Honolulu, HI, University of Hawaii at Manoa, 123–130.
- , and L. Hasse, 1992: Small-scale surface streaming under natural conditions as effective in air-sea gas exchange. *Tellus*, **44B**, 150–159.
- , and D. M. Farmer, 1999: Observations of the scale and occurrence of breaking surface waves. *J. Phys. Oceanogr.*, **29**, 2595–2606.
- , and —, 2004: Near-surface turbulence in the presence of breaking waves. *J. Phys. Oceanogr.*, **34**, 1067–1086.
- , T. D. Mudge, and V. D. Polonichko, 1994: On the energy input from wind to surface waves. *J. Phys. Oceanogr.*, **24**, 2413–2417.
- Gotwols, B. L., and G. B. Irani, 1980: Optical determination of the phase velocity of short gravity waves. *J. Geophys. Res.*, **85**, 3964–3970.
- Huang, N. E., Z. Shen, S. R. Long, M. C. Wu, Q. Zheng, N.-C. Yen, C. C. Tung, and H. H. Liu, 1998: The empirical mode decomposition and the Hilbert spectrum for nonlinear and non-stationary time series analysis. *Proc. Roy. Soc. London*, **454A**, 903–955.
- Hwang, P. A., D. W. Wang, E. J. Walsh, W. B. Krabill, and R. W. Swift, 2000: Airborne measurements of the wavenumber spectra of ocean surface waves. Part II: Directional distribution. *J. Phys. Oceanogr.*, **30**, 2768–2787.
- Jessup, A. T., and K. R. Phadnis, 2005: Measurement of the geometric and kinematic properties of microscale breaking waves from infrared imagery using a PIV algorithm. *Measurement Sci. Technol.*, **16**, 1961–1969.
- Kudryavtsev, V. N., V. K. Makin, and B. Chapron, 1999: Coupled sea surface-atmosphere model 2. Spectrum of short wind waves. *J. Geophys. Res.*, **104**, 7625–7639.
- Makin, V. K., V. N. Kudryavtsev, and C. Mastenbroek, 1995: Drag of the sea surface. *Bound.-Layer Meteor.*, **73**, 159–182.
- Melville, W. K., 1996: The role of surface-wave breaking in air-sea interaction. *Annu. Rev. Fluid Mech.*, **26**, 279–321.
- , and P. Matusov, 2002: Distribution of breaking waves at the ocean surface. *Nature*, **417**, 58–62.
- Monahan, E. C., and I. G. O'Muirheartaigh, 1986: Whitecaps and the passive remote sensing of the ocean surface. *Int. J. Remote Sens.*, **7**, 627–642.
- Phillips, O. M., 1985: Spectral and statistical properties of the equilibrium range in wind-generated gravity waves. *J. Fluid Mech.*, **156**, 505–531.
- , F. L. Posner, and J. P. Hansen, 2001: High range resolution radar measurements of the speed distribution of breaking events in wind-generated ocean waves: Surface impulse and wave energy dissipation rates. *J. Phys. Oceanogr.*, **31**, 450–460.
- Plant, W. J., 1982: A relationship between wind stress and wave slope. *J. Geophys. Res.*, **87**, 1961–1967.
- Terray, E. A., M. A. Donelan, Y. C. Agrawal, W. M. Drennan, K. K. Kahma, A. J. Williams III, P. A. Hwang, and S. A. Kitaigorodskii, 1996: Estimates of kinetic energy dissipation under breaking waves. *J. Phys. Oceanogr.*, **26**, 792–807.
- Thorpe, S. A., 1995: Dynamical processes of transfer at the sea surface. *Prog. Oceanogr.*, **35**, 315–352.
- Trevorrow, M. V., 1995: Measurement of ocean wave directional spectra using Doppler side-scan sonar arrays. *J. Atmos. Oceanic Technol.*, **12**, 603–616.

Copyright of *Journal of Physical Oceanography* is the property of *American Meteorological Society* and its content may not be copied or emailed to multiple sites or posted to a listserv without the copyright holder's express written permission. However, users may print, download, or email articles for individual use.